Current Opinion in Solid State and Materials Science 16 (2012) 39–44

Contents lists available at SciVerse ScienceDirect

Current Opinion in Solid State and Materials Science

journal homepage: www.elsevier.com/locate/cossms

Transmission electron microscopy of chalcogenide thin-film photovoltaic materials

Yanfa Yan *, Mowafak M. Al-Jassim

National Renewable Energy Laboratory, 1617 Cole Blvd., Golden, CO 80401, USA

ARTICLE INFO

Article history:
Received 3 February 2011
Accepted 16 October 2011
Available online 7 November 2011

Keywords:
TEM
Photovoltaic
Solar cell
CdTe
CIGS
Interface
Defect

ABSTRACT

Thin-film photovoltaic modules hold great promise to produce sustainable, low-cost, and clean electricity from sunlight, because thin-film solar cells can potentially be fabricated by economical, high-volume manufacturing techniques. However, to achieve high sunlight-to-electricity conversion efficiency, thin-film solar cells require sophisticated control on interface formation and materials qualities. Transmission electron microscopy (TEM) provides unique methods to access this information at the nanometer scale. In this paper, we provide a brief review on TEM studies of the interfaces, microstructure, and lattice defects in chalcogenide thin-film photovoltaic materials. We analyze the potential effects of the observed interface formation and materials quality that could affect the performance of solar cells.

1. Introduction

Chalcogenide thin-film photovoltaic (PV) materials, such as CdTe, Cu(In,Ga)Se_2 (CIGS), $Cu_2ZnSnSe_4$ (CZTSe), Cu_2ZnSnS_4 (CZTS), and $Cu_2ZnSn(S,Se)_4$ (CZTSSe), have attracted great attention for several decades [1–12] because of their potential for producing low-cost, high-efficiency, large-area thin-film solar cells. To date, the record solar-to-electricity conversion efficiencies for CdTe, CIGS, and CZTSSe-based solar cells have reached 16.7%, 20.3%, and 9.6%, respectively [6,10,12]. Chalcogenide thin-film solar cells typically consist of a front contact, *pn* junction, absorber layer, and back contact. To obtain high-efficiency solar cells, the contacts, *pn* junction, and absorber layer must be carefully engineered. Detailed information and understanding of extended defects, microstructure, chemistry, and interfaces of the solar cell materials are critical for device fabrication and engineering. The thickness of the layers in thin-film solar cells is in the range of micrometers, and transmission electron microscopy (TEM) has been an important and unique method to obtain information down to the nanometer scale that many other methods cannot achieve. In the past decades, TEM has been applied to investigate the microstructures and chemistry [1,13–20], interfaces [21–29], and structural defects such as stacking faults and grain boundaries [30–39], and phase separation [40], in thin-film chalcolgenide PV materials. The results have greatly helped in understanding the performance of thin-film solar cells. In this paper, we provide a brief review on TEM studies of chalcogenide thin-film materials including CdTe, Cu(In,Ga)Se_2, and $Cu_2ZnSn(S,Se)_4$. While high quality TEM images have been reported by many institutes and can be found in the references, the TEM images shown in this paper are all obtained from the materials synthesized at the National Renewable Energy Laboratory (NREL), which are intended to serve as examples.

2. TEM sample preparation

TEM sample preparation is crucial for TEM and scanning TEM (STEM) studies. Samples with large area and thickness less than 100 nm are usually preferred. There are three typical methods for TEM sample preparation: standard mechanical polishing, followed by Ar^+ ion milling; small angle cleavage technique (SACT) [41]; and focused ion beam (FIB) [42]. Each method has its advantages and disadvantages. The standard ion milling method can provide TEM samples with large thin regions. However, chalcogenide materials are usually sensitive to ion beam damage. The high-energy Ar^+ ion beam can sometimes introduce serious damage, such as the formation of additional lattice defects, the change of composition, and even phase transformation [43]. There are a few approaches have been commonly used to minimize Ar^+ ion beam induced damages. For example, the sample is thinned to very thin (below 2 μm) using a dimpler to reduce ion milling time. Low voltage ion milling is applied for final surface cleaning up. Samples are cooled to low temperature, usually liquid N_2 temperature, during ion milling. These approaches can reduce effectively ion beam induced surface damage. SACT is a relatively simple and inexpensive method for preparing cross sectional TEM samples by cleaving the thin film material. Therefore the TEM samples prepared by this method

* Corresponding author. Present address: Department of Physics, The University of Toledo, 2801 Bancroft Street, Toledo, OH 43606, USA.
E-mail address: Yanfa.yan@utoledo.edu (Y. Yan).

1359-0286/$ - see front matter © 2011 Elsevier Ltd. All rights reserved.
doi:10.1016/j.cossms.2011.10.001

are free from surface damage and contamination. However, the samples usually have relatively small electron transparent regions. Furthermore, the SACT technique cannot be used to prepare plan-view TEM samples. FIB method enables the preparation of large, uniformly thick, site-specific TEM samples. However, like the standard Ar^+ beam milling, FIB can also introduce surface damage and even causes Ga implantation. Therefore, careful final cleaning using a low energy Ga beam or a low voltage Ar^+ ion beam to remove the surface damage layer is usually needed.

3. Microstructures

Because CdTe absorber layers are typically deposited by the close-spaced sublimation (CSS) method, the deposited CdTe layer is always very close to stoichiometric. Therefore, there are very few studies on the stoichiometry of CdTe thin films. On the other hand, the phase diagram is very rich for Cu–In–Se-based compounds. For example, depending on the growth conditions, the deposited materials could be the α phase (chalcopyrite structure) $CuInSe_2$ (CIS), which is also called the 112 phase. The deposited materials could also be the β phase—ordered defect (Cu vacancy, V_{Cu}) chalcopyrite (ODC) structure—which has the composition of $CuIn_3Se_5$, or the γ phase (zinc-blende structure). The different phases have very different electronic properties. For example, the α phase is typically a p-type semiconductor, but the β phase is usually an n-type semiconductor. Knowing the microstructure of the deposited phase is critical for understanding the behavior of the fabricated CIGS thin-film solar cells. Therefore, most TEM studies of the microstructure have focused on CIS and its related materials. Notably, the University of Illinois has conducted the most systematic study on the ordering of point defects in epitaxially grown $CuInSe_2$ and $CuIn_3Se_5$ [1,14,15].

For high-efficiency CIGS solar cells, the CIGS layer should have the α phase. However, in some depositions, a small amount of β phase could co-exist. Because the α and β phases have similar structure and lattice constants, the co-existence of α and β phases cannot be identified easily by X-ray diffraction (XRD). Fortunately, the β phase has the ODC structure. The existence of a small amount of a β phase can be differentiated by convergent-beam electron diffraction (CBED), because the ordered structure should give extra diffraction spots in CBED patterns. For example, Fig. 1a shows a CBED pattern along the [1 1 0] zone axis taken from the α phase. To avoid overlap between diffraction discs, the smallest condenser lens aperture was used. As indicated by arrows, no extra diffraction spots are seen. Fig. 1b shows a CBED pattern along the [1 1 0] zone axis taken from an intentionally made very Cu-poor CIGS sample (Cu:(In,Ga):Se, 1:3:5). The bright spots are identical to those in Fig. 1a, indicating that the main structure is the chalcopyrite structure. However, additional weak spots, as indicated by arrows in Fig. 1b, are observed. These extra spots indicate that the phase contains ordered defects.

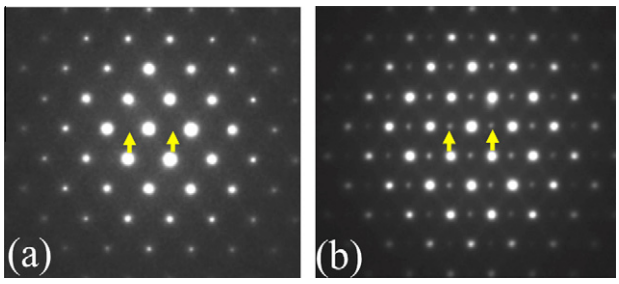

Fig. 1. Convergent-beam electron diffraction pattern taken from an (a) α chalcopyrite phase, and (b) chalcopyrite phase with ordered defects.

The advantage of CBED is that it can obtain structural information on the nanometer scale. It was suggested that high-efficiency CIGS solar cells have homojunctions—the surface layer of CIGS has the ODC structure (β phase). We have determined the structure from the surface and bulk regions in NREL's high-efficiency CIGS solar cells using CBED. No ODC structure was observed in either the surface or bulk regions. However, the surface layer is slightly more Cu-poor than the CIGS absorber, which may lead to different defect physics in the surface region.

TEM is also a powerful tool to examine local chemical compositions. For example, X-ray energy dispersive spectroscopy (EDS) has been used to examine the compositional change across grain boundaries in CIGS and CZTS thin films [39,40]. Here, strong chemical fluctuations at the nanometer scale that result in relatively Cu-poor and Cu-rich nanodomains from high-efficiency CIGS devices observed by STEM EDS profile is shown as an example [19]. Fig. 2a shows a low-resolution STEM high-angle annular dark-field image of a single CIGS grain. The image was formed by scanning a 1.4 Å electron probe across a specimen and recording the transmitted high-angle scattering with an annular detector. The intensity of the image can be described approximately as a convolution between the electron probe and an object function. Thus, the sample regions result in a bright contrast and the vacuum results in a dark contrast. Although the TEM samples were prepared carefully by cleaning the surface damage layer by ion milling using low voltage and low angle Ar^+ ion beam, a very thin layer with slight ion-beam-induced damage is expected to exist on both surfaces. Thus, we conducted a quantitative nanoscale EDS chemical analysis at relatively thick regions to minimize the effect on the composition from the slightly damaged surface layers. We first obtained EDS data at individual spots and, surprisingly, found that the compositions fluctuate strongly around the average composition, Cu:In:Ga:Se = 23.5:19:7:50.5, determined by electron-probe microanalysis (EPMA). The fluctuations were within ±6%, which is significantly larger than the system-detection error, i.e., normally smaller than ±2%. To verify whether these fluctuations were real, we carried out area-averaged EDS analysis by scanning the fine electron probe in selected areas, while acquiring EDS data. The averaged composition from the small square, which is about 50 nm × 50 nm, was Cu:In:Ga:Se = 24:14:8:54. The averaged composition from the large square, which is about 100 nm × 100 nm, was Cu:In:Ga:Se = 23:18:8:51, which is very close to the EPMA result. This indicates that the effect on the quantitative chemical compositions from the slightly damaged surface regions is negligible. We then carried out a series of individual EDS by a line profile along the black solid line in Fig. 2a. The line profile contained 15 individual data points separated equally by about 5 nm. At each data point, the chemical composition was quantified. In Fig. 2b, we plot the Cu/(In + Ga) and Ga/(In + Ga) ratios. The two dotted horizontal lines indicate the Cu/(In + Ga) and Ga/(In + Ga) ratios for the bulk composition. It is seen that both ratios fluctuate strongly at the nanoscale. Because the nanodomains are formed due to chemical fluctuations, they should be crystallographically coherent. Dislocations and other lattice defects do not have to form at the interfaces between the domains; rather, the interfaces will be smeared as a result of gradual interdiffusion.

The Cu/(In + Ga) ratio fluctuation may be understood as relatively Cu-poor and Cu-rich domains. If we assume that the Cu-poor domains exhibit n-type conductivity (electron-rich β-like domains) and the Cu-rich domains exhibit p-type conductivity (hole-rich α-like domains) [44], then the entire CIGS films are composed of nano *p–n* junction networks. Thus, the n-type networks can act as preferential electron pathways and the p-type networks can act as preferential hole pathways. The carriers generated by photons can be separated effectively, and separated carriers can be collected rapidly and efficiently into the electron and hole "freeways."

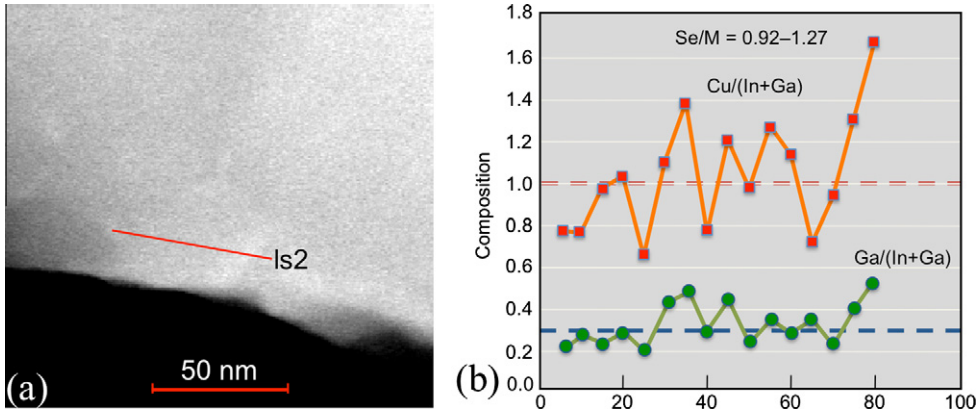

Fig. 2. (a) Z-contrast image taken from a thick region in a high-efficiency CIGS sample, and (b) profiles of Cu/(In + Ga) and Ga/(In + Ga) ratios.

[19,45] Because the domains are crystallographically coherent, electron–hole recombination rates are minimized for carriers collected across these intra-absorber junctions. As a result, the overall recombination can be effectively reduced.

4. Interfaces

The device structure of CIGS solar cells is typically Glass/Mo/CIGS/CdS/ZnO. Because the CdS layer is usually deposited at room temperature, no interdiffusion between CIGS and CdS is expected. Therefore, TEM studies on the CIGS/CdS interface are very limited, except for a few reports [26–28,39]. In these studies, the thickness uniformity and coverage of CdS layers were examined. However, during the deposition of the CIGS layer at high temperature, an interfacial layer, $MoSe_2$, is formed between Mo and CIGS. The formation of the $MoSe_2$ layer, which is a good p-type conductor, is regarded as beneficial for cell performance because it helps to form a good ohmic contact. Therefore, TEM studies of the $MoSe_2$ layer have been reported by many research groups [21–24]. The unique feature of the $MoSe_2$ layer is the layered structure, shown in Fig. 3a. EDS taken from the circled area, shown in Fig. 3b, confirms the formation of the $MoSe_2$ layer. The Mo back contact layer is typically grown on glass substrates by sputtering or evaporation methods and often exhibits the columnar grain morphology. The $MoSe_2$ layer is found to follow closely the surface of the Mo layer, leading to excellent contact with the Mo back contact.

TEM studies of interfaces in CdTe solar cells are more focused on the CdTe/CdS junction. This is because CdTe solar cells typically have the superstrate cell structure, Glass/FTO/CdS/CdTe/back contact. The CdTe layer is deposited on CdS at high temperature, usually above 500 °C. It is known that at such temperatures, interdiffusion would occur between CdTe and CdS. The interdiffusion leads to the formation of $CdS_{1-x}Te_x$ regions [29]. It is found that the presence of oxygen in the CdS layers dramatically affects the interdiffusion behavior.

The CdS can be grown by various methods, such as chemical-bath deposition (CBD) and CSS. The CdTe/CdS solar cells with CdS films grown by these methods can have different performance. Normally, the CBD CdS films give better cell performance than the CdS films grown by the other techniques. However, the CSS growth method is more applicable to large-scale manufacturing. CBD CdS has a high concentration of impurities, mainly O, whereas CdS grown by other techniques has much less O, unless O is intentionally introduced. It has been reported that the presence of O_2 during the deposition of the CSS CdS improves open-circuit voltage (V_{oc}) by up to 50 mV. It is also reported that the thermal annealing of CdS in air drastically increases efficiency. Thus, it is likely that the high O concentration in CBD CdS films is responsible for the better device performance.

To investigate the effects of oxygen on the interdiffusion at CdS/CdTe junctions, we have grown CdTe and CdS layers on SnO_2-coated Si wafers. The CdS films with a thickness of about 150 nm were grown by CBD and CSS with various O pressures. The thickness of the SnO_2 layer was about 0.5 μm. The CdTe films were grown by CSS without the presence of O. The CdTe source temperature was 660 °C, and the substrate temperature was 620 °C. The thickness of the CdTe films was about 8 μm. Samples with only CdS deposited were used as thickness references for understanding the consumption and reaction of CdS at the junction. The microstructure of the CdS/CdTe junctions was examined by TEM.

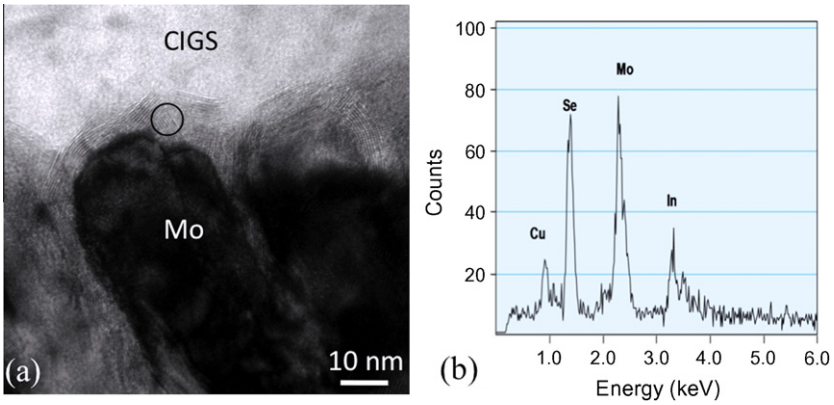

Fig. 3. (a) TEM image of Mo/CIGS interface. (b) EDS taken from the interface region (circle) showing the formation of $MoSe_2$.

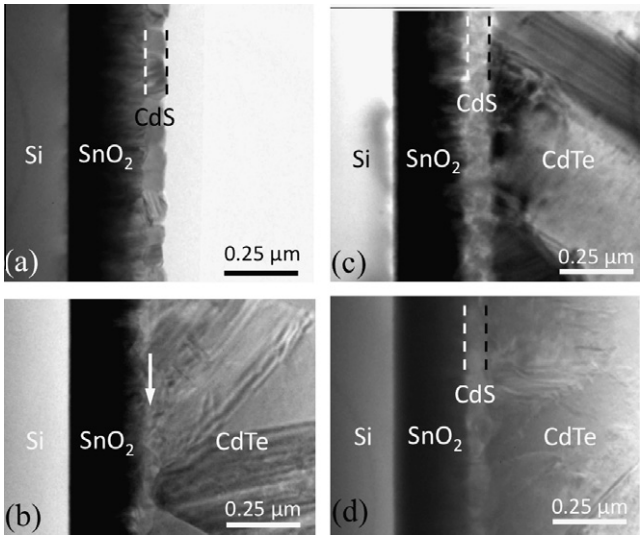

Fig. 4. Cross-sectional TEM images of (a) as-deposited CdS layer, (b) CdS/CdTe interface for CdS deposited without the presence of O, (c) CdS/CdTe interface for CdS deposited with the presence of O, and (d) CdS/CdTe interface for CdS deposited without the presence of oxygen, but annealed in oxygen for 10 min.

Fig. 4a shows a cross-sectional TEM image of a CdS layer deposited without the presence of oxygen. The thickness of the CdS layer is about 100 nm. Fig. 4b and c show cross-sectional TEM images of CdS/CdTe junctions with CdS films deposited with zero and 2.5 torr O pressures, respectively. As seen in Fig. 4a, the CdS layer should be about 100 nm before the deposition of CdTe, but it is not seen clearly in some regions (see Fig. 4b). This indicates that during the deposition of CdTe (620 °C), strong interdiffusion occurred between CdS and CdTe in the sample with the CdS layer deposited without the presence of O, and the CdS layer is consumed by the interdiffusion. In some regions, the CdTe seems to contact directly the SnO_2 layer (as indicated by the arrow), showing a complete consumption of CdS near the junction. In some regions, the CdS layer is observed, but with significantly decreased thickness.

EDS taken with a small probe size of 20 nm from the thickness-reduced CdS region indicates that the CdS has converted to $CdS_{1-x}Te_x$ alloy. In the CdTe side, $CdTe_{1-x}S_x$ alloys were found near the junction. However, in Fig. 4c, in which the CdS layer was deposited with 2.5 torr O pressure, the CdS layer is clearly seen and its thickness is almost the same as the CdS layer in the reference sample (without a CdTe film). EDS data showed that $CdS_{1-x}Te_x$ alloys can only be found near the junction. As the distance from the junction increases, the concentration of Te decreases rapidly. This indicates that the interdiffusion is much weaker in the CdS/CdTe junction with the CdS layer deposited with the presence of O. In other words, the presence of O in the CdS layer significantly suppresses the interdiffusion at the CdS/CdTe junction. To verify this conclusion, we annealed the CSS-CdS thin film in an oxygen environment at 400 °C for 10 min to incorporate oxygen into CdS. After the annealing, CdTe was deposited at the same condition. With the annealing, the CdS layer is now seen clearly, as shown in Fig. 4d, confirming that the presence of oxygen in CdS significantly suppresses the interdiffusion at the CdS/CdTe interface.

We have also examined CdS/CdTe junctions with the CdS layer grown by CBD. It is known that the CBD CdS films have a different structure and contain large amounts of impurities, including a high concentration of O. A cross-sectional TEM image (not shown) of a CdS/CdTe junction with CBD CdS layer clearly revealed the CdS layer. Similar to Fig. 4c, the thickness of CdS is not changed significantly after the deposition of CdTe. EDS data also showed $CdS_{1-x}Te_x$ alloys near the junction, and the concentration of Te decreases rapidly with the increase of distance from the junction. Thus, the CdS/CdTe junction with CBD CdS demonstrates that it is O that suppresses the interdiffusion at CdS/CdTe junctions.

The presence of O in CdS also affects the diffusion of S along grain boundaries in CdTe. It is found that if both CdS and CdTe were deposited in the presence of O, the diffusion of S along grain boundaries is minor. However, if both CdS and CdTe are deposited without the presence of O, the diffusion of S along the grain boundaries in CdTe is very significant [34]. The strong interdiffusion results in completely consumed CdS regions and the formation of $CdS_{1-x}Te_x$ alloys with high Te concentration. The effects of completely consumed CdS regions are similar to that of pinholes. This leads to a reduced V_{oc} and short-circuit current density (J_{sc}) due to its increased electrical shorting of the junction. The $CdS_{1-x}Te_x$ alloys have a lower energy bandgap than CdS and the bandgap changes with Te concentration. The bandgap of $CdS_{1-x}Te_x$ decreases very quickly with an increase of Te concentration. Thus, strong interdiffusion will form a thick lower-bandgap $CdS_{1-x}Te_x$ layer. This layer, which absorbs more photons than CdS, will result in a blue loss. This also decreases the J_{sc}. Thus, when O is present in CdS films, all these problems can be overcome by suppressing the interdiffusion. In addition, the $CdTe_{1-x}S_x$ alloy can also decrease the mismatch between the CdS and CdTe, leading to reduced interface states. Thus, to some degree, interdiffusion is helpful to cell performance. Hence, an optimized oxygen concentration in the CdS layer would improve the CdS/CdTe solar cell efficiency.

TEM has also been used to study the back-contact of CdTe solar cells. Fabricating high quality back-contact for CdTe solar cells usually requires etching of the CdTe surface using mixed nitric and phosphoric (NP) acids prior to applying the back contact, because this process can improve the series resistance. NP etching is known to deplete the crystalline CdTe surface of Cd and create a Te-rich layer. TEM has been used to investigate this Te rich layer after NP etching (an example is shown in Fig. 5a). The best back-contact

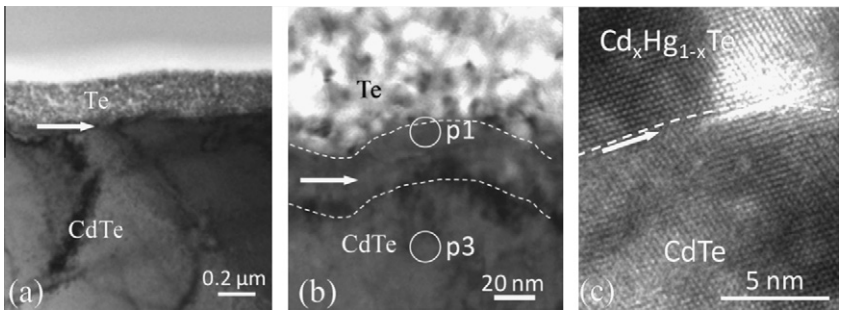

Fig. 5. Cross-sectional TEM images of CdTe back junction. (a) CdTe with NP etching. (b) Interface between CdTe and Te layer. (c) HRTEM image of the interface region at CdTe/Te.

was also achieved by applying (HgTe, CuTe)-graphite paste to the etched surface. It is found that this process facilitates the formation of an intermediate layer between the CdTe and Te layers [6], as indicated by the arrow in Fig. 5b. This intermediate layer was found to contain high concentration of Hg. NP etching is known to deplete Cd, forming Cd-poor CdTe, which is energetically unfavorable. Therefore, Hg may diffuse from the (HgTe, CuTe)-graphite paste into this region to occupy Cd vacancies to form $Cd_xHg_{1-x}Te$. The structure of $Cd_xHg_{1-x}Te$ should be similar to CdTe and should have an epitaxial relationship with CdTe. Because Cu is very mobile in CdTe, much Cu was found in this intermediate layer. To verify the epitaxial relationship, we investigated the microstructure of a single-crystal CdTe film after NP etching and (HgTe, CuTe)-graphite pasting, because a single crystal allows us to perform high-resolution TEM more easily. We found that the effects of NP etching and (HgTe, CuTe)-graphite pasting on single-crystal CdTe film are the same as on polycrystalline CdTe films. Fig. 5c is a HRTEM image obtained from the CdTe/$Cd_xHg_{1-x}Te$ interface from the CdTe single crystal. The electron beam is along the [110] zone axis of CdTe. The composition of $Cd_xHg_{1-x}Te$ is confirmed by EDS. The white dashed line indicates the interface, which can only be estimated from the contrast because there is no abrupt interface. The epitaxial relationship is seen clearly from the HRTEM image.

The formation of an epitaxial $Cd_xHg_{1-x}Te$ layer on CdTe is critical for forming a high-quality back contact on CdTe. Because of the epitaxial relationship, the density of interface states at the CdTe/$Cd_xHg_{1-x}Te$ interface will be very low. In addition, both $Cd_xHg_{1-x}Te$ and Te are known to be excellent p-type conductors. We may assume that there is no barrier between the $Cd_xHg_{1-x}Te$ and Te valence-band maxima. Thus, the hole-barrier at the CdTe/$Cd_xHg_{1-x}Te$/Te structure will be much smaller. The formation of the epitaxial $Cd_xHg_{1-x}Te$ layer may improve hole flow at the back contact, and hence, reduce the series resistance of the CdTe solar cell device.

5. Structural defects

TEM has been used to identify the atomic structure and chemistry of defects such as stacking faults, twins, dislocations, and grain boundaries in both CdTe and CIGS thin films [29–37]. Using the combination of HRTEM, image simulation, and density-functional theory (DFT), the atomic structure and electronic properties of these defects are obtained [34,35]. It was found that stacking faults and lamellar twins do not contain dangling bonds, and therefore, do not create deep levels; thus, they are not extremely harmful. However, grain boundaries are found to contain both Cd and Te dangling bonds, which create deep levels and cause nonradiative recombination and thus are harmful.

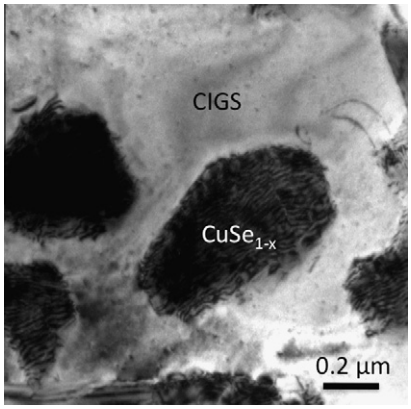

Fig. 7. TEM sample of CIGS showing the formation of secondary-phase, $CuSe_{1-x}$.

Fig. 6 shows an example of how the grain-boundary structures are determined by using the combination of HRTEM, image simulation, and DFT. The atomic structure of two grain boundaries are first constructed based on the HRTEM images shown in Fig. 6c and d. These structure models are then relaxed using DFT calculations. Their optimized structures are shown in Fig. 6a and b, respectively. The blue (dark color) balls indicate Cd atoms, whereas the gray (light color) balls indicate Te atoms. These two structures—called DP(1) and DP(2), respectively—look similar, but have different details. For example, in DP(1), in Fig. 6a, the atom numbered "3" has four bonds and Te numbered "2" has a dangling bond. But in DP(2), the atom numbered "3" has four bonds and Te numbered "2" has a dangling bond. The two structurally optimized models are used for HRTEM image simulations. The experimental parameters are obtained by through-focus and through-thickness simulations of the HRTEM image of the perfect

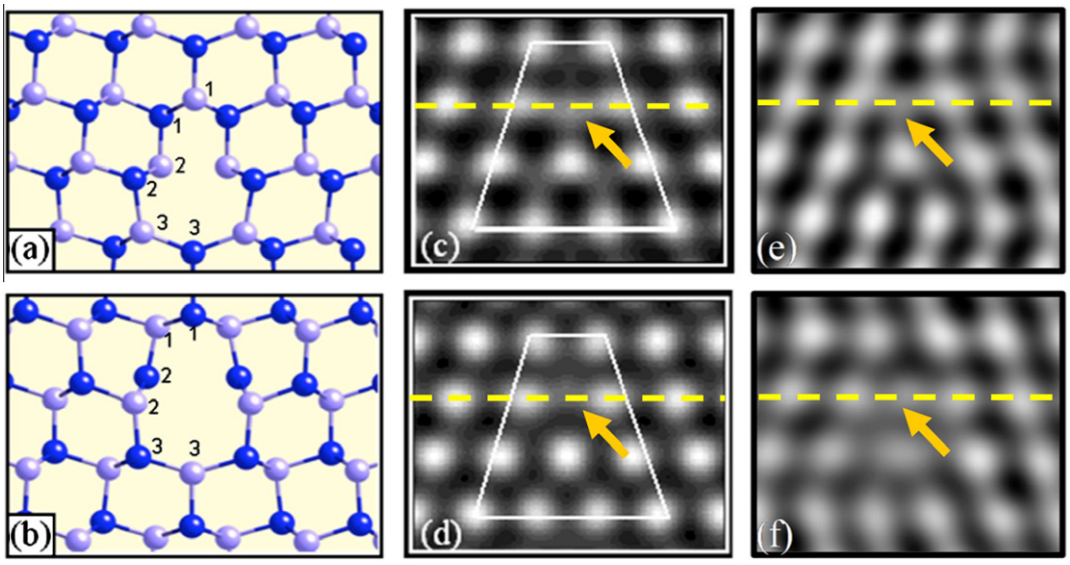

Fig. 6. (a and b) Optimized DP(1) and DP(2) structure models. The black balls indicate Cd atoms, and the gray balls indicate Te atoms. (c and d) Simulated HRTEM image using DP(1) and DP(2) structure models. (e and f) HRTEM images of two boundaries that match the simulated images.

regions near the boundary. Fig. 6c and d are the simulated images using the structural models of Fig. 5a and b, respectively. For these simulations, these images are seen to fit with two HRTEM images, Fig. 6e and f, obtained from DP twin boundaries. DFT calculations also revealed that these grain boundaries exhibit deep levels in the bandgap of CdTe. The details can be found in Ref. [34].

6. Phase separation

The formation of secondary phases is very harmful for thin-film solar cells. However, for multinary compound materials such as CIGS and CZTS, the formation of a secondary phase is possible. For example, Cu_xSnS_y has been found in CZTS [40]. The secondary phases can often form inside the absorber materials. TEM is a good technique to view the location of the secondary phases. For example, if a Cu-rich CIGS film is grown, a secondary phase of $CuSe_{1-x}$ will typically form. The location of $CuSe_{1-x}$ particles embedded in a CIGS grain is shown in Fig. 7. The black particles are $CuSe_{1-x}$ particles, as confirmed by EDS analysis, which showed only Cu and Se peaks. Because no In and Ga signals were detected from the $CuSe_{1-x}$ particles, the $CuSe_{1-x}$ particles likely partially penetrate the grains of the CIGS films, or the Cu_xSe particles are embedded in the large CIGS grains. Diffraction patterns from these particles and the surrounding CIGS revealed that the $CuSe_{1-x}$ particles and the CIGS have similar diffraction patterns; they also have an epitaxial relationship, where $CuSe_{1-x}$ particles adopt the structure of CIGS when they are embedded in CIGS.

7. Future directions

This brief review has shown that TEM is a powerful technique to provide information on the microstructure and chemistry of defects, interfaces, and junctions in polycrystalline thin-film solar cells. However, TEM based techniques have the ability to provide much more information. For example, electron energy loss spectroscopy (EELS), and cathodoluminescence (CL) and electron-beam-induced current (EBIC) can provide electronic information of solar cell materials. This information can provide significant insight for understanding the performance of thin film solar cells. We think an integrated TEM system with the capability of EELS, EDS, CL, and EBIC will play an even more important role in the research of PV materials, because such an system enables the mapping of the structural, chemical, electrical, optical, and electronic information from the same location. Such integration has been very difficult, because TEM with high spatial resolution does not have the volume needed to integrate additional tools. However, with the rapid progress of aberration-corrected TEMs, which offer large space for integration and yet maintain high special resolution, the integrated TEM system should become available in the near future.

Acknowledgements

The authors are grateful to P. Shelton, R. Noufi, D. Albin, X. Li, T. Gessert, K. Jones, W. Stanbery, and S. Pennycook for providing samples used in this study and/or fruitful discussions. The research was supported by the US Department of Energy under Contract No. DE-AC36-08GO28308.

References

[1] Rocket A, Birkmire RW. J Appl Phys 1991;70:R81.
[2] Britt J, Ferekides C. Appl Phys Lett 1993;62:2851.
[3] Herberholz R, Nadenau V, Ruehle U, Koeble C, Shock HW, Dimmler B. Sol Energy Mater Sol Cells 1997;49:227.
[4] Ohyama H, Aramoto T, Kumazawa S, Higuchi H, Arita T, Shibutani S, et al. In: Proc 26th IEEE photovoltaic specialists conference. IEEE, New York; 1997. p. 343.
[5] Ferekides CS, Marinskiy D, Viswanathan V, Tetali B, Paleski V, Selvaraj P, et al. Thin Solid Films 2000;361–362:520.
[6] Wu X, Keane JC, Dhere RG, Dehart C, Duda A, Gessert TA, et al. In: Proceedings of the 17th European photovoltaic solar energy conference. Munich, 22–26, October 2001. p. 995–1000.
[7] Wu X. Sol Energy 2004;77:803.
[8] Katagiri H. Thin Solid Films 2005;480:426.
[9] Repins I, Contreras MA, Egaas B, DeHart B, Scharf J, Perkins CL, et al. Prog Photovolt: Res Appl 2008;16:235.
[10] Todorov TK, Reuter KB, Mitzi DB. Adv Mater 2010;22:1.
[11] Guo Q, Ford GM, Yang W-C, Walker BC, Stach EA, Hillhouse HW, et al. J Am Chem Soc 2010;132:17384.
[12] Green MA, Emery K, Hishikawa Y, Warta W. Prog Photovolt: Res Appl 2011;19:84.
[13] Tseng BH, Rockett A, Lommasson TC, Yang LC, Wert CA, Thornton JA. J Appl Phys 1990;67:2637.
[14] Xiao HZ, Yang LC, Rockett A. J Appl Phys 1994;76:1503.
[15] Hasoon FS, Yan Y, Althani H, Jones KM, Moutinho HR, Alleman J, et al. Thin Solid Films 2001;387:1.
[16] Yan Y, Jones KM, Abushama J, Young M, Asher S, Al-Jassim MM, et al. Appl Phys Lett 2002;81:1008.
[17] Moutinho HR, Albin D, Yan Y, Dhere RG, Li X, Perkins C, et al. Thin Solid Films 2003;436:175.
[18] Durose K, Asher AE, Jaegermann W, Levi D, McCandless BE, Metzger W, et al. Prog Photovolt: Res Appl 2004;12:177.
[19] Yan Y, Noufi R, Jones KM, Ramanathan K, Al-Jassim MM, Stanbery BJ. Appl Phys Lett 2005;87.
[20] Weber A, Schmidt S, Abou-Ras D, Schubert-Bischoff P, Denks I, Mainz R, et al. Appl Phys Lett 2009;95:041904.
[21] Wada T. Sol Energy Mater Sol Cells 1997;49:249.
[22] Nishiwaki S, Kohara N, Negami T, Wada T. Jpn J Appl Phys 1998;37:L71.
[23] Wurz R, Marron DF, Meeder A, Rumberg A, Babu SM, Schedel-Niedrig Th, et al. Thin Solid Films 2003;431:398.
[24] Assmann L, Bernede JC, Drici A, Amory C, Halgand E, Morsli M. Appl Surf Sci 2005;246.
[25] Yan Y, Dhere RG, Jones KM, Al-Jassim MM. J Appl Phys 2001;89:5944.
[26] Abou-Ras D, Kostorz G, Romeo A, Rudmann D, Tiwari AN. Thin Solid Films 2005;480–481:118.
[27] Abou-Ras D, Kostorz G, Atrohn A, Schock HpW, Tiwari AN. J Appl Phys 2005;98:123512.
[28] Cojocaru-Miredin O, Choi P, Wuerz R, Raabe D. Appl Phys Lett 2011;98:103504.
[29] Ferekides CS, Balasubramanian U, Mamazza R, Viswanathan V, Zhao H, Morel DL. Sol Energy 2004;77:823.
[30] Yan Y, Al-Jassim MM, Jones KM, Wei S-H, Zhang SB. Appl Phys Lett 2000;77:1461.
[31] Yan Y, Al-Jassim MM. Thin Solid Films 2001;389:75.
[32] Al-Jassim MM, Yan Y, Moutinho HR, Romero MJ, Dhere RD, Jones KM. Thin Solid Films 2001;387:246.
[33] Yan Y, Albin D, Al-Jassim MM. Appl Phys Lett 2001;78:171.
[34] Yan Y, Al-Jassim MM, Jones KM. J Appl Phys 2003;94:2976.
[35] Yan Y, Noufi R, Al-Jassim MM. Phys Rev Lett 2006;96:205501.
[36] Yan Y, Jiang C-S, Noufi R, Wei S-H, Moutinho HR, Al-Jassim MM. Phys Rev Lett 2007;99:235504.
[37] Lei C, Li CM, Rockett A, Robertson I. J Appl Phys 2007;101:024909.
[38] Siebentritt S, Eisenbarth T, Rockett A, Albert J, Schubert-Bischoff P, Lux-Steiner MCh. J Phys: Condens Matter 2007;19:016004.
[39] Lei C, Duch M, Robertson IM, Rockett A. J Appl Phys 2010;108:114908.
[40] Wang K, Shin B, Reuter KB, Todorov T, Mitzi DB, Guha S. Appl Phys Lett 2011;98:051912.
[41] McCaffrey JP. Ultramicroscopy 1991;38:149.
[42] Giannuzzi LA, Stevie FA, editors. Introduction to focused ion-beams: instrumentation, theory, techniques and practice. NewYork, USA: Springer; 2005.
[43] Yan Y, Jones KM, Noufi R, Al-Jassim MM. Thin Solid Films 2007;515:4681.
[44] Contreras MA, Wiesner H, Matson R, Tuttle J, Ramanathan K, Noufi R. Mater Res Soc Symp Proc 1996;426:243. and references therein.
[45] Stanbery BJ. In: Proceedings of the 31st IEEE photovoltaics specialists conference. IEEE, New York; 2005. p. 355.